Analysis of the Radar Channel and Its Variability in Vital-Sign Sensing Applications

Bartosz Tegowski, Dominik Langer, *Graduate Student Member, IEEE*,
Nils C. Albrecht, *Graduate Student Member, IEEE*, and Alexander Koelpin, *Fellow, IEEE*

***Abstract*—In millimeter-wave (mmWave) radar-based vital-sign sensing, the radar sensor usually operates in the radiative near field of the target, which is the human body. Therefore, in contrast to far-field conditions, scattering cannot be quantified by a target-inherent radar cross section (RCS) as it strongly depends on the relative position and directivity of the radar antenna. To investigate the resulting consequences for the application, this article examines the radar channel transfer function, i.e., the ratio between the power waves feeding and being received by the antenna, with particular focus on its variability due to changes of the relative antenna position. The analysis is supported by a physical-optics-based simulation model tailored to practical circumstances. Measurements at 24 GHz and 61 GHz using antennas with different directivities and a human-like mannequin as a target confirm the simulative predictions. The radar channel suffers from significant variations, e.g., displacing the antenna by less than 1 mm can cause a 30-dB receive power drop. A statistical analysis comprehensively evaluates the radar channel variability and clarifies the challenges for the application that stem from target near-field effects.**

***Index Terms*—Channel modeling, near-field effects, physical optics (PO), radar cross section (RCS), radar theory, vital-sign sensing, wave propagation.**

I. Introduction

THE application of radar technology for the remote sensing of vital signs has received much attention in the past decades. Breathing and heart activity introduce deformations and vibrations of the human body, which can be sensed by radar and related to physiological parameters via signal processing. Operating without physical contact with the patient, the radar-assisted monitoring is considered beneficial since it does not impair the patient's regular behavior.

Although systems operating in the single-digit gigahertz range are applicable to monitor the breathing activity [1], the trend goes toward higher operating frequencies in the millimeter-wave (mmWave) band [2]–[4]. This is motivated by the increase of sensitivity required to identify subtle vibrations associated with the pulse wave and in particular the heart sounds. The latter allow for a more precise time-domain determination of individual heart beats [5], which is paricularly important to extract advanced physiological features such as the heart-rate variability (HRV), i.e., the time difference between the onset times of consecutive heart cycles. Here, missing or inaccurate detections are critical. For operation in a medical environment, the systems are often accommodated in the industrial, scientific and medical (ISM) bands, e.g., at 24 GHz or 61 GHz [6], [7].

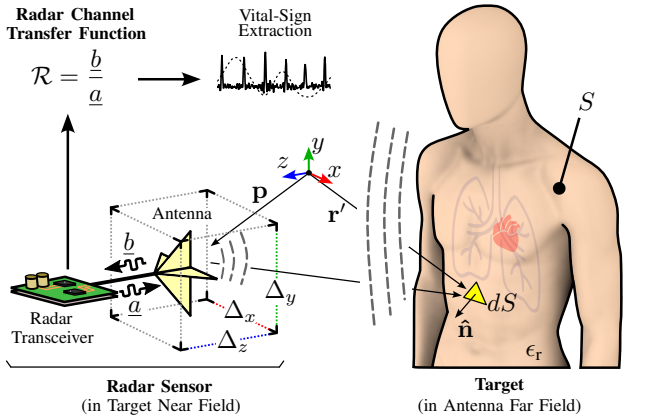

Fig. 1. Generic radar-based vital-sign sensing configuration consisting of the human body as target and a monostatic radar sensor based on an antenna and a radar transceiver.

Independent of the body deformation associated with the vital signs, a living subject unintentionally changes its relative position and orientation with respect to the radar sensor during a practical measurement. Consequently, as indicated in Fig. 1, the relative antenna position can be considered undetermined and random within a particular volume (Δ_x,Δ_y,Δ_z). Even though proof-of-concept measurements validate the fundamental feasibility of radar-based vital-sign sensing, they seldom address the reliability and robustness for long-term usage in versatile conditions, where random variations of the relative alignment inevitably occur.

Research in the topic of vital-sign sensing has been dominated by the investigation of different use-cases, signal processing techniques, and radar architectures [8] including continuous-wave (CW) [7], [9], [10], frequency-modulated CW (FMCW) [4], [11], or ultra-wideband systems [12]. However, the evident prerequisite for successful radar-based vital-sign sensing is the determination of the complex-valued radar channel transfer function $\mathcal{R}$, i.e., the transmission from the transmit to the receive antenna due to scattering by the human body target, as indicated in Fig. 1. The vital signs and

Received 10 August 2025; revised 04 November 2025; accepted 27 November 2025. This work was supported in part by the Deutsche Forschungsgemeinschaft (DFG, German Research Foundation)-SFB 1483, EmpkinS under Project-ID 442419336. (*Corresponding author: Bartosz Tegowski.*)

The authors are with the Institute of High-Frequency Technology, Hamburg University of Technology, 21073 Hamburg, Germany (e-mail: bartosz.tegowski@tuhh.de; dominik.langer@tuhh.de; nils.albrecht@tuhh.de; alexander.koelpin@tuhh.de).

Digital Object Identifier XX.XXXX/TAP.202X.XXXXXXX

other unassociated deformations of the target shape introduce a time-dependent variation of $\mathcal{R}$ from which the vital signs are subsequently deduced. Thus, the analysis of the superordinate scattering and wave propagation effects, which is presented in this article, is key to identify challenges and to understand physical limitations, which are independent of particular radar architectures or signal processing techniques.

Since the radar antenna is typically located at a distance smaller or comparable to the human body dimensions the illuminated target area usually measures several tens of wavelengths at mmWave frequencies and, thus, is electrically large. Even if the target is in the far field of the antenna, the radar sensor then operates in the radiative near field of the target (referred to as *target near field* in the following), which is why the target cannot be considered a point target. Accordingly, the classical understanding of a range- and antenna-independent radar cross section (RCS), which is inherent to the target, is not applicable. Analyses of the angle-dependent RCS of a human body, known from automotive radars [13], are not meaningful. Instead, the antenna-target system requires a conjoint analysis because the antenna directivity also impacts the scattering effects due to its inhomogeneous target illumination and weighted reception [14]. In addition, the antenna selects the portion of the body whose temporal-deformations are related to physiological effects [2], [15], [16].

In the target near field, phenomena such as power level fading and nonlinear phase distortion dominate the scattering properties [14]. To analyze these effects and their practical consequences for the vital-sign sensing application, electromagnetic simulations are beneficial as they provide well-defined and controllable conditions, which is not feasible in measurements with living subjects. The simulation should account for the dominant effects, but at the same time, it sould be computationally simple to examine a multitude of different configurations. The large electrical size of the human body makes full-wave simulations not reasonably applicable as they suffer from a high computational effort [17]. Ray-tracing techniques [18], [19] as well as simplified target models based on canonical shapes [20] are an alternative at the expense of accuracy. Physical-optics-based concepts provide a good trade-off between physical accuracy and computational complexity. They can handle lossy dielectric target materials [21], [22] and they can be extended from their conventional far-field formulation [22] to work within the target near field [14], [23]–[25], also in the case of human-body targets [24], [25]. Even though the evaluation of the scattered fields suffices to define the near-field RCS [26], [27] analogous to the classical far-field RCS definition [22], the complex-valued radar channel transfer function $\mathcal{R}$ encompasses the nonnegligible effect of the antenna radiation pattern and, thus, provides the complete characterization needed for this application [14], [25].

Because of the large electrical size of the human body at mmWave frequencies, even small variations of the relative position may already significantly modulate the measured return signal thereby impairing robustness of the vital-sign sensing. In this context, this article examines the variability of the radar channel transfer function upon varying relative position of the radar antenna. The analysis is performed by means of the physical-optics-based complex-valued transfer function from [14], which is extended to lossy dielectric materials to account for the electromagnetic properties of skin. A discussion of the skin material properties justifies practical simplifications. With the focus on the general scattering characteristics arising in a typical vital-sign sensing setup and their experimental validation, a representative static human body model is considered. The variability of both magnitude and phase of the transfer function is evaluated statistically, which provides a comprehensive representation of the scattering effects identifying the physical challenges for vital-sign sensing applications independent of a particular radar system architecture and signal processing.

The article is organized as follows. Section II deals with the calculation of the radar channel transfer function including an analysis of the skin material properties and the justification of practical simplifications. Section III presents simulation and measurement results for various configurations. Section IV provides a statistical analysis of the results. Section V concludes the article.

II. Determination of the Radar Channel Transfer Function

This section presents the approach used to simulate the radar response for mmWave vital-sign sensing applications. It aims to account for the dominant scattering effects while reducing the computational effort and the level of detail required for modeling. Disregarding the presence of clothes or blankets, the human skin is the first interface the electromagnetic wave interacts with. Thus, it is necessary to first discuss its material properties and clarify its impact on the scattering properties. In the next step, the derivation of the radar channel is addressed following the concept initially presented in [14] and [25], including the introduction of practical simplifications.

A. Material Properties of Skin and Related Simplifications

The human skin is commonly considered as a smooth, homogeneous, lossy dielectric being characterized by the relative complex-valued permittivity $\epsilon_\mathrm{r} = \epsilon_\mathrm{r}' - \mathrm{j}\epsilon_\mathrm{r}'' = \epsilon_\mathrm{r}'(1 - \mathrm{j}\tan(\delta))$, where $\tan(\delta) = \epsilon_\mathrm{r}''/\epsilon_\mathrm{r}'$ refers to the loss tangent [28], [29] and $\mathrm{j} = (-1)^{0.5}$ denotes the imaginary unit. In literature, different works provide Cole-Cole models for ϵ_r based on measured tissue samples [30]–[32]. Models by Gabriel *et al.* [31] distinguish between dry and wet skin, whereas those by Sasaki *et al.* [32] consider different skin layers, i.e., the epidermis and the dermis. Fig. 2 presents the relative permittivity in a frequency range from 1 GHz to 100 GHz according to these models. Regardless of the absolute discrepancies, they qualitatively behave very similarly over frequency. The real part of the relative permittivity decays with increasing frequency. Above 10 GHz, the loss tangent increases with frequency reaching a plateau around 60 GHz. At 24 GHz and 61 GHz, the relative permittivity (loss tangent) amounts to $\epsilon_\mathrm{r}' \approx 20$ $(\tan(\delta) \approx 0.65)$ and $\epsilon_\mathrm{r}' \approx 9$ $(\tan(\delta) \approx 0.9)$, respectively.

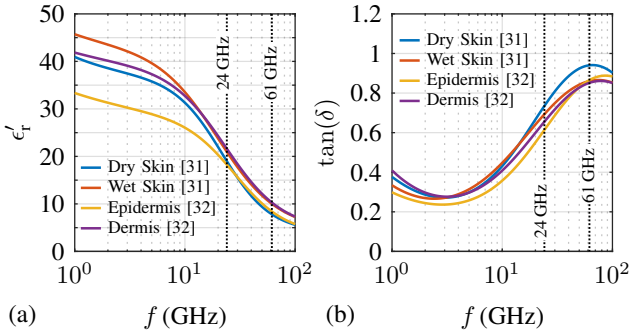

Fig. 2. (a) Real part of the relative permittivity and (b) loss tangent of skin based on Cole-Cole models by Gabriel *et al.* [31] by Sasaki *et al.* [32].

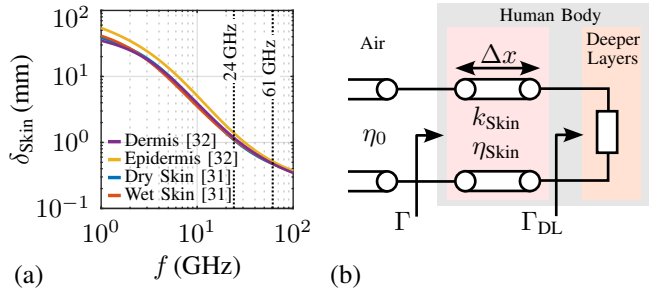

Fig. 3. (a) Penetration depth δ_{Skin} based on skin permittivity models by Gabriel [30] by Sasaki [32]. (b) Transmission line model of the air-body interface.

From the application viewpoint, variations of the permittivity due to individual skin conditions and properties are natural, which makes exact permittivity values not relevant. Nonetheless, the models indicate the range for the skin permittivity.

1) Penetration Depth: Because of the high loss tangent a significant amount of the wave refracted into the skin will be absorbed. Fig. 3(a) evaluates the $1/e$-penetration depth

$$\delta_{\text{Skin}} = \frac{1}{\text{Re}(\text{j}k_{\text{Skin}})} = \frac{1}{\omega\sqrt{\mu\epsilon_0\epsilon'_{\text{r}}}}\sqrt{\frac{2}{\sqrt{1+\tan^2(\delta)}-1}} \quad (1)$$

for the considered models. It derives from the wavenumber

$$k_{\text{Skin}} = \omega\sqrt{\mu_0\epsilon_0\epsilon'_{\text{r}}}\sqrt{1-\text{j}\tan(\delta)} \quad (2)$$

of a lossy dielectric [33]. μ_0 and ϵ_0 denote the vacuum permeability and permittivity, respectively. With increasing frequency, the penetration depth decreases. Above 20 GHz, the penetration depth drops below 2 mm and amounts to about 0.5 mm at 61 GHz. Thus, the penetration depths are in the order of typical skin thickness, which typically amounts to a few millimeters [28].

2) First-Interface-Reflection Simplification: Fig. 3(b) shows a transmission line model of the air-human-body interface, where plane wave conditions are assumed. The homogeneous skin layer is characterized by its wavenumber k_{Skin}, its intrinsic impedance $\eta_{\text{Skin}} = \omega\mu_0/k_{\text{Skin}}$, and thickness Δx.[1] The effect of deeper layers (fat, muscles, bones, etc.) is summarized by the reflection coefficient Γ_{DL}. A wave imping on the air-skin interface experiences the reflection coefficient Γ, which results from impedance transformation.

[1]The biological structure of skin consists of multiple layers (stratum corneum, epidermis, dermis, subcutaneous tissue), which have similar dielectric properties. Thus, for an electromagnetic approximation, skin is treated as a homogeneous layer.

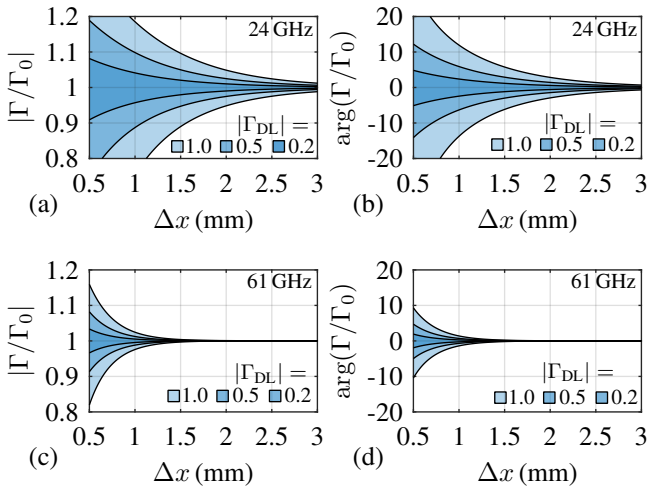

Fig. 4. Relative variation of (a) and (c) the magnitude, and (b) and (d) the phase of the reflection coefficient Γ depending on the skin thickness Δx and the reflection coefficient of deeper layers Γ_{DL} for (a) and (b) 24 GHz, and (c) and (d) 61 GHz. The epidermis permittivity model [32] is assumed. The shaded areas indicate the variation of $0 \leq \arg\{\Gamma_{\text{DL}}\} < 2\pi$.

To quantify whether the modeling of the human body for mmWave vital-sign sensing applications can be limited to the reflection at the very first air-skin interface, i.e.,

$$\Gamma_0 = \Gamma|_{\Gamma_{\text{DL}}=0} = \frac{\eta_{\text{Skin}} - \eta_0}{\eta_{\text{Skin}} + \eta_0}, \quad (3)$$

Fig. 4 evaluates Γ relative to Γ_0 versus skin thickness Δx for different Γ_{DL} based on the epidermis model [32]. $\eta_0 = (\mu_0/\epsilon_0)^{0.5}$ is the intrinsic impedance of free space. For generality, the phase of Γ_{DL} covers all values $0 \leq \arg(\Gamma_{\text{DL}}) < 2\pi$ and the resulting ratio $\Gamma_{\text{DL}}/\Gamma_0$ is indicated by the shaded area with the maximum and minimum envelopes marked by solid lines for both magnitude and phase.

Even in the theoretical worst-case approximation, i.e., the homogeneous skin layer is terminated by a reflective load ($|\Gamma_{\text{DL}}| = 1$), the deviation relative to the reflection at the first interface is less than $\pm 5\,\%$ in terms of amplitude and within $\pm 2°$ in terms of phase evaluated for a skin thickness $\Delta x > 2$ mm at 24 GHz. At 61 GHz, significantly smaller deviations result due to the smaller penetration depth. Here, the aforementioned deviations are not exceeded for a thickness $\Delta x > 0.95$ mm. However, since the permittivity of other biological material, e.g., fat, muscles, bones, etc., is comparable to that of skin [31], the deviations are expected to be significantly smaller in practice due to smaller $|\Gamma_{\text{DL}}|$ defined by the permittivity contrast, as indicated in Fig. 4.

Consequently, for radar applications at mmWave frequencies, the interaction between the incident wave and the human body can be reasonably limited to the first reflection at the air-skin interface. The refracted wave can be considered absorbed and not to contribute to scattering. This accords with the common assumption made for far-field RCS analysis in the context of automotive radars [29].

B. Radar Channel Transfer Function

The human torso is electrically large at mmWave frequencies, does not exhibit edges, and its radii of curvature are larger than the wavelength. These properties make physical optics well suitable to determine the radar channel with a significantly lower computational effort in comparison to full-wave simulations. As shown in [14] for perfect electric conductor (PEC) targets, the antenna radiation pattern can be incorporated to account for the effects in the target near field. This subsection first extends the concept from [14] to targets with a homogeneous lossy dielectric material. Following the analysis of Section II-A2, it is assumed that only the scattering at the first material interface needs to be accounted for. In the second step, the scattering due to a highly lossy dielectric, such as skin, is compared with the scattering in the case of PEC.

1) Derivation: Fig. 1 defines the considered setup. The goal is to derive the transfer function $\mathcal{R} = \underline{b}/\underline{a}$ between the power wave $\underline{a}$ that feeds the antenna and the received power wave $\underline{b}$. The starting point of the derivation is the general expression for the scattered magnetic field [22, Eq. (2.2-20)] ($\exp(\mathrm{j}\omega t)$ time dependence)

$$\mathbf{H}_{\text{sca}}(\mathbf{r}) = -\frac{1}{4\pi}\int_S \Big[-\mathrm{j}\frac{k}{\eta}(\hat{\mathbf{n}}\times\mathbf{E})\psi_0 - (\hat{\mathbf{n}}\times\mathbf{H})\times\nabla\psi_0 - \langle\hat{\mathbf{n}},\mathbf{H}\rangle\nabla\psi_0\Big]dS \tag{4}$$

following the Stratton-Chu integrals [22]. In (4), $\mathbf{E}$ and $\mathbf{H}$ denote the total electric and magnetic field strengths at the closed target surface S, respectively, k is the wavenumber in the environmental medium and η its intrinsic impedance, $\hat{\mathbf{n}}$ is the outward pointing unit normal vector of the surface element dS, and

$$\psi_0 = \frac{\exp(-\mathrm{j}k|\mathbf{r}-\mathbf{r}'|)}{|\mathbf{r}-\mathbf{r}'|} \tag{5}$$

is Green's function of free space, where $\mathbf{r}'$ describes the position of dS and $\mathbf{r}$ is the position at which the scattered field is to be evaluated. $\langle\cdot,\cdot\rangle$ denotes the scalar product. Furthermore, the gradient operating on $\mathbf{r}'$ reads (assuming $k|\mathbf{r}-\mathbf{r}'| \gg 1$)

$$\nabla\psi_0 \approx \mathrm{j}k\psi_0\cdot\hat{\mathbf{s}} \tag{6}$$

where

$$\hat{\mathbf{s}} = \frac{\mathbf{r}-\mathbf{r}'}{|\mathbf{r}-\mathbf{r}'|}. \tag{7}$$

Accordingly, inserting (5)–(7) in (4), the scattered field is

$$\mathbf{H}_{\text{sca}}(\mathbf{r}) = \frac{\mathrm{j}k}{4\pi}\int_S \psi_0\mathbf{X}dS \tag{8}$$

where

$$\mathbf{X} = \frac{1}{\eta}(\hat{\mathbf{n}}\times\mathbf{E}) + (\hat{\mathbf{n}}\times\mathbf{H})\times\hat{\mathbf{s}} + \langle\hat{\mathbf{n}},\mathbf{H}\rangle\hat{\mathbf{s}}. \tag{9}$$

The total fields at the scatterer surface are approximated invoking the tangent-plane approximation [22]. At each surface patch dS, one assumes that it extends infinitely according to its tangent plane. Furthermore, presuming that the target is in the antenna far field, the field incident on dS

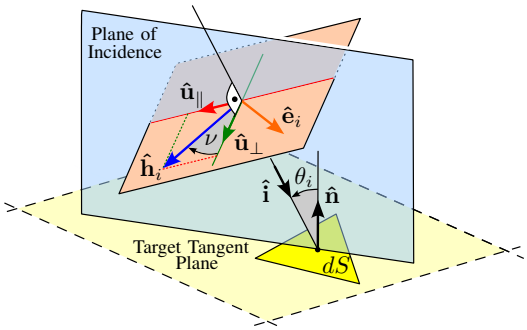

Fig. 5. Definitions at the plane of incidence and the tangent plane.

$$\mathbf{H}_{\text{inc}} = \underbrace{\mathrm{j}\underline{a}\sqrt{\frac{G(\mathbf{r}')}{4\pi\eta|\mathbf{r}'-\mathbf{p}|^2}}e^{-\mathrm{j}[k|\mathbf{r}'-\mathbf{p}|-\Psi(\mathbf{r}')]}}_{=H_{\text{inc}}}\cdot\hat{\mathbf{h}}_i \tag{10}$$

is considered to locally appear as a plane wave. Its magnitude $|H_{\text{inc}}|$, phase $\arg\{H_{\text{inc}}\}$, and orientation $\hat{\mathbf{h}}_i$ follow from the far-field radiation pattern (gain pattern G, phase pattern Ψ) of the radar antenna and spherical wave propagation. $\mathbf{p}$ denotes the antenna position. Using fundamental relationships for plane wave reflection at a dielectric interface [22], the total fields at the scatterer surface are approximated by the sum of the incident and the reflected plane waves, i.e.,

$$\mathbf{H} = H_{\text{inc}}\left\{\cos(\nu)(1+\Gamma_H)\hat{\mathbf{u}}_\perp + \sin(\nu)[\hat{\mathbf{u}}_\parallel + \Gamma_E(\hat{\mathbf{o}}\times\hat{\mathbf{u}}_\perp)]\right\} \tag{11}$$

$$\mathbf{E} = \eta H_{\text{inc}}\left\{\sin(\nu)(1+\Gamma_E)\hat{\mathbf{u}}_\perp - \cos(\nu)[\hat{\mathbf{u}}_\parallel + \Gamma_H(\hat{\mathbf{o}}\times\hat{\mathbf{u}}_\perp)]\right\} \tag{12}$$

with $\hat{\mathbf{i}} = (\mathbf{r}'-\mathbf{p})/|\mathbf{r}'-\mathbf{p}|$ denoting the unit vector of incidence and $\hat{\mathbf{o}} = \hat{\mathbf{i}} - 2\langle\hat{\mathbf{i}},\hat{\mathbf{n}}\rangle\hat{\mathbf{n}}$ follow from Snell's law. Here, the directions of the incident magnetic ($\hat{\mathbf{h}}_i$) and electric ($\hat{\mathbf{e}}_i = \hat{\mathbf{h}}_i\times\hat{\mathbf{i}}$) fields are decomposed by the polarization angle ν in the contributions perpendicular ($\hat{\mathbf{u}}_\perp$) and parallel ($\hat{\mathbf{u}}_\parallel$) to the plane of incidence, as defined in Fig. 5. The reflected fields are accordingly weighted by the Fresnel reflection coefficients [33]

$$\Gamma_E = \frac{\eta'\cos\theta_i - \sqrt{1-\eta'^2(1-\cos^2\theta_i)}}{\eta'\cos\theta_i + \sqrt{1-\eta'^2(1-\cos^2\theta_i)}} \tag{13}$$

and

$$\Gamma_H = \frac{\cos\theta_i - \eta'\sqrt{1-\eta'^2(1-\cos^2\theta_i)}}{\cos\theta_i + \eta'\sqrt{1-\eta'^2(1-\cos^2\theta_i)}} \tag{14}$$

where $\eta' = \eta_{\text{Skin}}/\eta_0$ and $\cos\theta_i = -\langle\hat{\mathbf{n}},\hat{\mathbf{i}}\rangle$ is determined by the angle of incidence θ_i. The total fields in the region not visible from the perspective of the antenna are set to zero [22]. Possible reflections between different parts of the target are considered insignificant to alter the fundamental properties of the radar channel. These could be accounted for by an iterative approach [24].

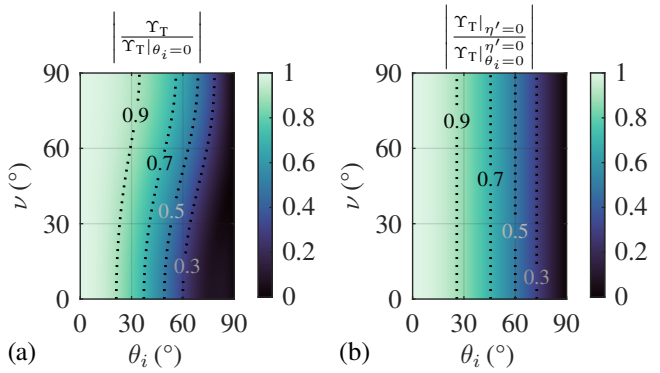

Fig. 6. Normalized magnitude of the integrand contribution Υ_T versus relative polarization angle ν and angle of incidence θ_i in the case of (a) skin (epidermis model [32]) at 61 GHz and (b) PEC ($\eta' = 0$).

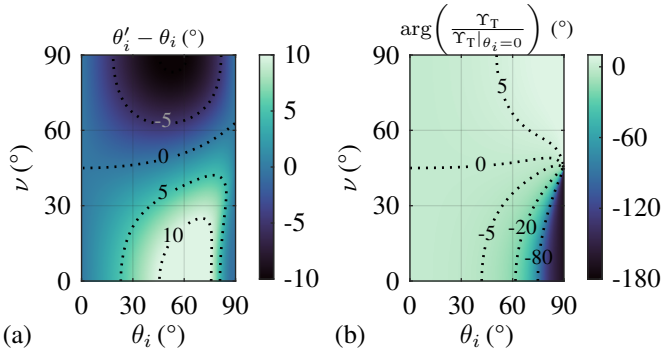

Fig. 7. (a) Angle of incidence difference between a PEC and a skin (epidermis model [32] at 61 GHz) surface patch required to match the relative magnitudes of their integrand contributions Υ_T. (b) Normalized phase of the integrand contribution Υ_T versus relative polarization angle ν and angle of incidence θ_i in the case of the epidermis permittivity model [32]) at 61 GHz.

To determine the received power wave $\underline{b}$, the scattered field is evaluated at the position of the receive antenna. Assuming that the scattering contribution from each dS appears as a plane wave, it is individually weighted according to the effective antenna area by $(\pi\eta G)^{1/2}/k$ and the phase shift $\exp(j\Psi)$ due to the phase pattern. Thus, for a monostatic configuration, $\mathbf{r} = \mathbf{p}$, $\hat{\mathbf{s}} = -\hat{\mathbf{i}}$, and following (8) one obtains

$$\underline{b} = \frac{\mathrm{j}k}{4\pi} \int_S \psi_0 \frac{\sqrt{\pi\eta G(\mathbf{r}')}}{k} e^{\mathrm{j}\Psi(\mathbf{r}')} \langle \mathbf{X}, \hat{\mathbf{h}}_i \rangle dS \tag{15}$$

where the scalar product $\langle \mathbf{X}, \hat{\mathbf{h}}_i \rangle$ accounts for co-polarization matching. Presuming a single-polarized antenna, the cross-polarization is disregarded. Combining the relationships (5), (7), and (9)–(14) in (15), and exploiting the vector triple product identity together with the orthogonality relationships at the plane of incidence, one obtains the radar channel transfer function

$$\mathcal{R} = \frac{\underline{b}}{\underline{a}} = \int_{\bar{S}} \underbrace{G(\mathbf{r}') e^{2\mathrm{j}\Psi(\mathbf{r}')}}_{=\Upsilon_A} \cdot \underbrace{\frac{e^{-2\mathrm{j}k|\mathbf{r}'-\mathbf{p}|}}{4\pi|\mathbf{r}'-\mathbf{p}|^2}}_{=\Upsilon_{FS}} \cdot \Upsilon_T \, d\bar{S} \tag{16}$$

as a definite integral over the lit part of the target surface $\bar{S}$. The integrand in (16) $\Upsilon = \Upsilon_A \cdot \Upsilon_{FS} \cdot \Upsilon_T$ is factorized in the antenna characteristic term Υ_A, the spherical free-space propagation term Υ_{FS}, and

$$\Upsilon_T = \langle \hat{\mathbf{n}}, \hat{\mathbf{i}} \rangle \left[\Gamma_H \cos^2(\nu) - \Gamma_E \sin^2(\nu) \right] \tag{17}$$

which is the contribution associated with the relative target shape and material properties.

2) Perfect-Electric-Conductor Approximation: Fig. 6(a) evaluates the magnitude of the integrand contribution Υ_T versus all possible angles of incidence θ_i and relative polarization angles ν, exemplarily, for the epidermis permittivity model [32] at 61 GHz. It is normalized to the value at normal incidence $|\Upsilon_T|_{\theta_i=0}| = 0.603$, which corresponds to the maximum value of $|\Upsilon_T|$. The dependence on ν, which results from the dielectric material, is less distinctive than the dependence on θ_i. For reference, Fig. 6(b) shows the magnitude of the normalized integrand contribution in the case of PEC material. Here, $\eta' = 0$, $\Gamma_H = -\Gamma_E = 1$ and the integrand contribution simplifies to $\Upsilon_T|_{\eta'=0} = \langle \hat{\mathbf{n}}, \hat{\mathbf{i}} \rangle$, which is independent of the relative polarization angle.

Comparing Fig. 6(a) with (b), the normalized integrand contributions for the lossy dielectric and PEC show similar behavior over the entire domain of ν and θ_i. This similarity can be exploited to assume PEC as representative of the dielectric skin model in terms of the resulting radar channel transfer function. This practical simplification would facilitate its analysis as well as the experimental validation because of a well-defined material and the omission of polarization.

To justify the applicability of this simplification in a general way, consider a surface patch dS with skin dielectric material and a surface patch dS' with PEC material. Their orientation with respect to the antenna is identical and leads to arbitrary $\theta_i \in [0, \pi/2]$ and $\nu \in [0, \pi/2]$. Because of the different material properties, their integrand contributions are not equal within the domain of θ_i and ν. However, if the PEC surface patch dS' would be tilted such as to generate an angle of incidence

$$\theta_i' = \arccos\left(\frac{\left|\Gamma_H \cos^2(\nu) - \Gamma_E \sin^2(\nu)\right|}{|\Gamma_H|_{\theta_i=0}|} \cos(\theta_i) \right) \tag{18}$$

instead of θ_i, the integrand magnitudes would satisfy $|\Upsilon_T(\theta_i, \nu)| = |\Upsilon_T|_{\eta'=0}(\theta_i', \nu)||\Gamma_H|_{\theta_i=0}| \; \forall \theta_i, \nu$. Thus, dS and dS' would produce equal integrand magnitudes except for the constant scaling factor $|\Gamma_H|_{\theta_i=0}|$, which accounts for the overall signal attenuation due to absorption. Fig. 7(a) evaluates the required change in angle of incidence. It is below $\pm 13°$ over the entire domain of polarization angles and angles of incidence. In addition, also the integrand phase related to dS and dS' must match for equivalence of the radar channel transfer functions according to (16). In the case of PEC, the integrand phase is constant and independent of θ_i and ν. Fig. 7(b) evaluates the phase of Υ_T normalized to the phase at normal incidence in the case of the epidermis model at 61 GHz. The gradually changing phase stems from dielectric losses. This dependence could be imitated by a translative shift of the PEC surface patch dS' by $\arg\{\Upsilon_T\}/(2k)$, which is not larger than a quarter of the wavelength.

In conclusion, the monostatic scattering from skin and PEC is very comparable based on the homogeneous skin permittivity model. The fundamental scattering effects will be related to the overall shape, size, and orientation of

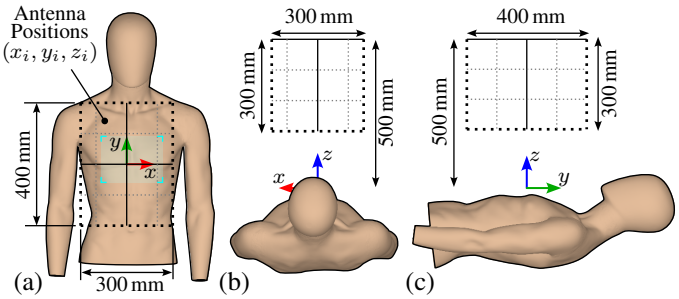

Fig. 8. Exemplary human-body-like target and definition of the Cartesian coordinate system. The rectangular areas marked by the dotted contour define the domain of antenna positions in the (a) xy-, (b) the xz-, and (c) the yz-planes. The drawings are true to scale. The region in (a) highlighted in cyan is used for the statistical evaluation in Section IV.

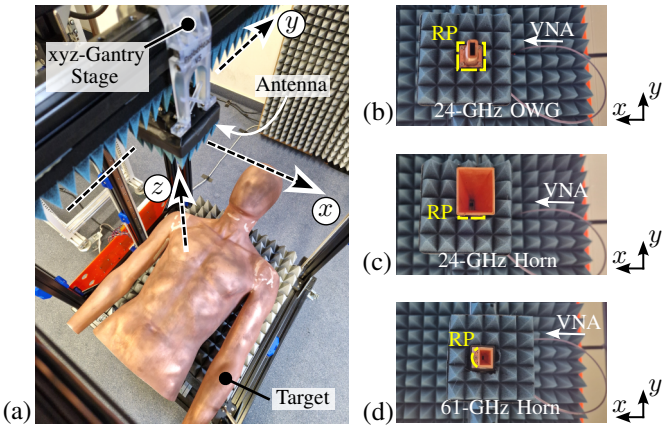

Fig. 9. (a) Measurement setup and (b)–(d) the antennas used.

the target rather than its material properties. The minor virtual modifications of the target shape required to equalize the radar channel transfer functions of a skin and a PEC target are insufficient to distort the cardinal shape of a human body. Furthermore, in the context of vital-sign sensing, the actual target shape is individual to each patient and, thus, not to known. It can be considered random to some extent. Consequently, the exact consideration of a particular target shape including the correct materials is not purposeful. The analysis of the radar channel transfer function and its variability at mmWaves for this application can thus be studied by assuming PEC as a reasonable representative of skin. Absorption effects can be accounted for by rescaling the amplitude of the radar channel transfer function in proportion to the Fresnel reflection coefficient magnitude (14) evaluated at normal incidence. This is consistent with exemplary results encountered in discussions of automotive radars [29]. Note that other materials between the human skin and the antenna such as clothes, blankets, or mattresses are disregarded in this article. However, if not significantly thinner than the wavelength, they can introduce additional effects [34]. In addition, the PEC approximation neglects depolarization, which stems from the dielectric properties of the target. Its consdieration would require a dual-polarized antenna, which is outside the scope of the considered configuration.

III. Variability of the Radar Channel – Simulation and Measurement Results

This section investigates the variability of the radar channel transfer function $\mathcal{R}$ for varying antenna positions and different antenna directivties in simulation and measurement. For this, the representative configuration from Fig. 8 is considered. An exemplary human-like body model serves as target. It is considered static without incorporating dynamic motions associated with vital signs because the superordinate goal is to analyze the fundamental properties of the radar channel and its variability as it occurs in a vital-sign sensing configuration. The estimation of vital-sign parameters is not the scope of this article. The temporal evolution of the radar channel due to vital-sign-related motion would lead to slightly different target shapes at each sampling instance without altering its fundamental relationships stemming from the operation in the target near field. To examine the effect of antenna directivity an 18-dBi pyramidal horn and a 9-dBi open-ended waveguide (OWG) are considered as antennas at 24 GHz. In addition, a 61-GHz 18-dBi pyramidal horn is used to demonstrate the impact of frequency. The position of the antenna (x_i, y_i, z_i) is varied in the xy-, yz- and the xz-planes, as indicated in Fig. 8. At each position, the radar channel transfer function is determined.

Fig. 9 presents the measurement setup that implements the configuration from Fig. 8. The target is based on an copper-coated off-the-shelf mannequin whose 3D-CAD model (shown in Fig. 8) is obtained by a *Zeiss Atos Compact Scan* 3D-scanner. The 3D-printed and metallized antennas, see Fig. 9(b)-(d), and the mannequin target are mounted in a three-axis gantry stage. It positions the antenna in the xy-plane and controls the distance between the antenna and the target by moving the latter along z-direction. The antenna E-plane is parallel to the xz-plane. A waveguide-to-coaxial adapter and a coaxial cable connect the antenna to a vector network analyzer (VNA) (*Agilent Technologies E8361A*). The VNA measures the input reflection coefficient S_{11} at each position (x_i, y_i, z_i), from which the radar channel transfer function $\mathcal{R}$ is obtained. The VNA is calibrated with respect to the antenna waveguide flange reference plane (RP), indicated in Fig. 9(b)-(d), using an Open-Short-Match (OSM) calibration. Simulation results are based on (16) with PEC target material and full-wave simulated far-field patterns of the antennas.

A. Results for Variation in the xy-Plane

The antenna positions are set on a rectlinear grid within $|x| \leq 0.15\,\text{m}$ and $|y| \leq 0.2\,\text{m}$, see Fig. 8(a). A 4-mm step width is selected and the results are upsampled to an 0.5-mm grid by spline interpolation of the real and imaginary parts of $\mathcal{R}$. The xy-plane is at $z = 500\,\text{mm}$. In measurement, the inherent antenna input reflection coefficient and reflections from the measurement setup add up to the reflection associated with the target. To compensate for this, the target is moved at each sampling position (x_i, y_i) along z-direction in the range of 10 mm (4 mm) in the case of 24 GHz (61 GHz) in five equidistant steps. At each step, S_{11} is measured. The center of

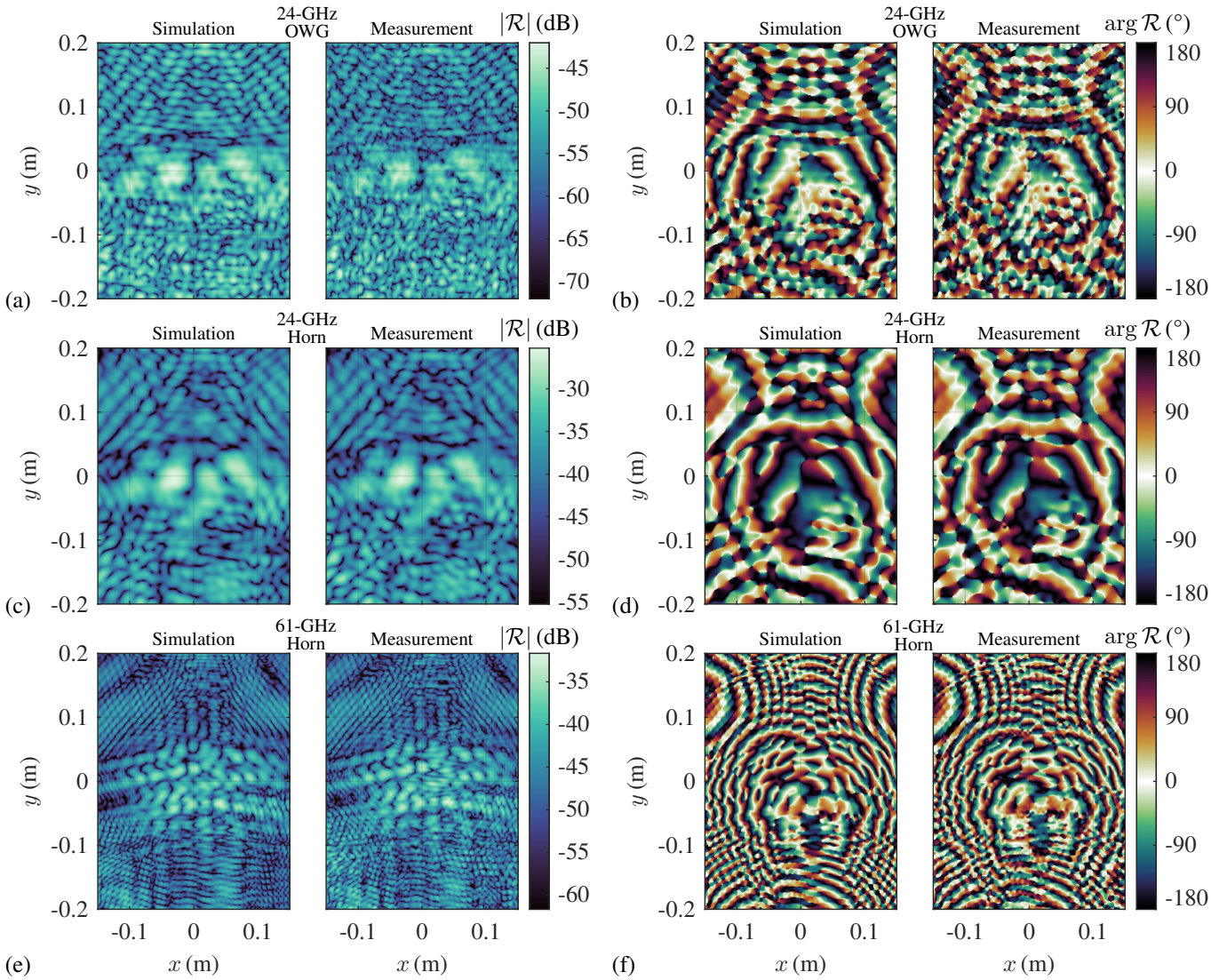

Fig. 10. Simulated and measured radar channel transfer function $\mathcal{R}$ in the xy-plane at $z = 500\,\text{mm}$ in the case of (a) and (b) an OWG at 24 GHz, (c) and (d) a horn antenna at 24 GHz, and (e) and (f) a horn antenna at 61 GHz. (a), (c), and (e) Magnitude (the colorbar spans a 30-dB dynamic range and its upper limit is set by the maximum simulated value). (b), (d), and (f) Phase.

the circle fitted to these five reflection coefficients estimates the contribution of the clutter reflection, which is subtracted from S_{11} to yield the radar channel transfer function $\mathcal{R}(x, y)$.

Fig. 10(a) and (b) shows the simulated and measured radar channel transfer function at 24 GHz for an OWG in terms of magnitude [Fig. 10(a)] and phase [Fig. 10(b)]. The magnitude is subject to excessive fading, which even exceeds 30 dB. It rapidly varies within the considered observation window. Changes of the antenna position in the order of some millimeters already lead to significant variations of the receive power level. Similarly, the phase is strongly varying. Positions of abrupt phase changes align with those where receive power level drops by orders of magnitude. The agreement between simulation and measurement for both magnitude and phase validates the calculation according to (16). In addition to the agreement with respect to the overall xy-dependence, the absolute values match well. Remaining discrepancies stem from alignment, directivity, and target model uncertainties, imperfect clutter removal, and multipath propagation effects

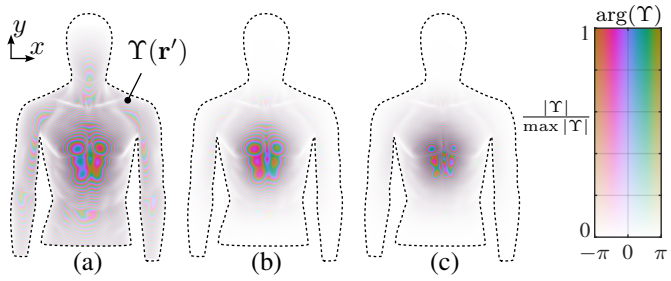

Fig. 11. Complex-valued integrand Υ on target surface for (a) the 24-GHz OWG, (b) the 24-GHz horn, and (c) the 61-GHz horn. The phase is represented by colors, whereas the opacity level indicates the magnitude normalized to the maximum value. The antenna is at $(x, y, z) = (0, 0, 0.5\,\text{m})$.

including the antenna self-RCS [35], [36].

To investigate the impact of the antenna directivity, Fig. 10(c) and (d) presents the results obtained for a horn antenna at 24 GHz. Despite identical antenna positions as in the OWG-measurement, a different response $\mathcal{R}(x, y)$

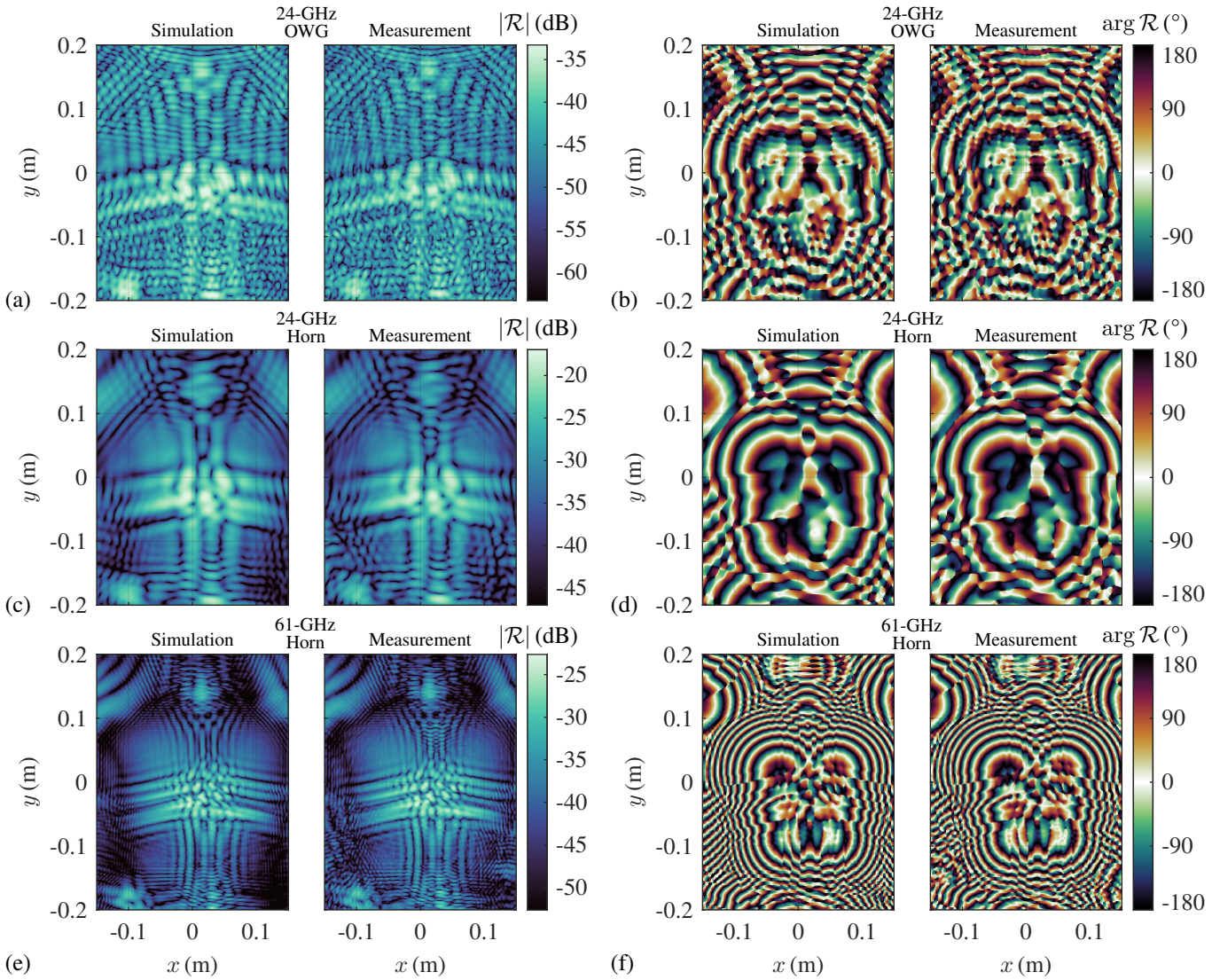

Fig. 12. Simulated and measured radar channel transfer function $\mathcal{R}$ in the xy-plane at $z = 200$ mm in the case of (a) and (b) an OWG at 24 GHz, (c) and (d) a horn antenna at 24 GHz, and (e) and (f) a horn antenna at 61 GHz. (a), (c), and (e) Magnitude (the colorbar spans a 30-dB dynamic range and its upper limit is set by the maximum simulated value). (b), (d), and (f) Phase.

is obtained. This evidences that the radar antenna has a nonnegligible impact on the resulting scattering properties when operating in the target near field. This is contrary to far-field conditions where the target RCS is uniquely attributed to the target and, thus, antenna-independent. Compared to the OWG-measurement, the higher directivity of the horn, in addition to a higher overall magnitude level, leads to a slower varying radar channel transfer function. Nonetheless, power fading may still exceed 30 dB. As confirmed by both simulation and measurement, the higher directivity improves the phase flatness.

The difference between the OWG- and the horn-configuration is due to different weighting introduced by the projection of the radiation pattern on the target surface. Fig. 11(a) and (b) plots the complex-valued integrand Υ on the corresponding target surface elements in the case of the OWG and the horn, respectively. The antennas are at $(x, y, z) = (0, 0, 500)$ mm. Following the notation in (16), the free-space and target-shape terms Υ_{FS} and Υ_{T} are identical in both cases. The difference is introduced by the different antenna characteristic terms Υ_{A}. The higher directivity fades out the outer portions of the target. Thus, depending on the antenna, a different effective target results. Consequently, in the case of the horn, the effective target has a smaller electromagnetic extent and the radar sensor operates closer to the target far field, which leads to slower variations.

Fig. 10(e) and (f) shows the radar channel transfer function at 61 GHz for a horn antenna with the 18-dBi directivity. The increase in frequency leads to a faster variation of the receive power level and phase. This is because of the increased electrical size of the target. Fig. 11(c) presents the integrand Υ over the target surface. Compared to the 24-GHz case [Fig. 11(b)], the change is mainly due to the free-space term Υ_{FS}, whose phase more rapidly varies over the target surface because of the shorter wavelength.

Further evaluations are conducted in the xy-plane at $z = 200$ mm. Fig. 12 presents the simulation and measurement results for the same configuration of antennas.

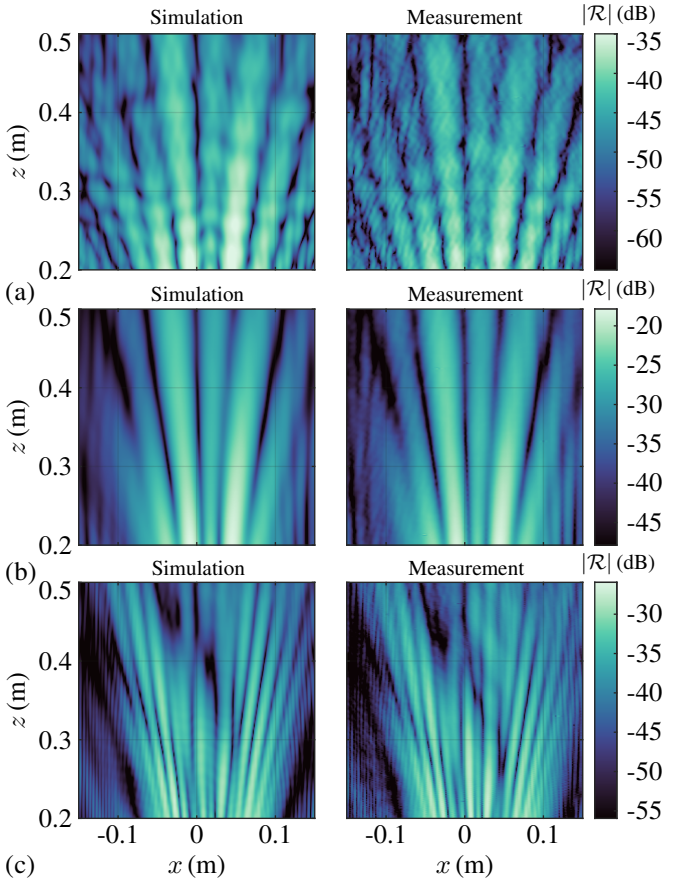

Fig. 13. Simulated and measured magnitude of the radar channel transfer function $\mathcal{R}$ in the xz-plane at $y = 0$ in the case of (a) a 24-GHz OWG, (b) a 24-GHz horn, and (c) a 61-GHz horn antenna. The colorbar spans a 30-dB dynamic range and its upper limit is set by the maximum simulated value.

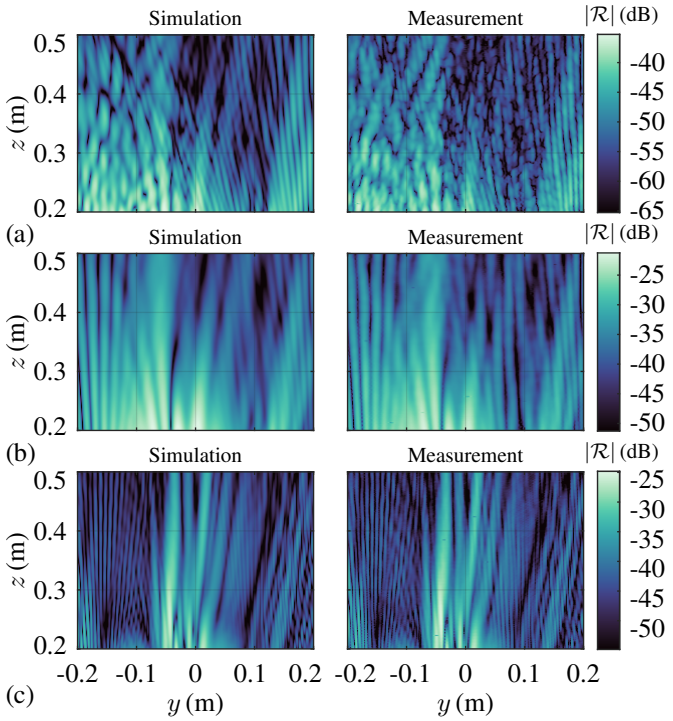

Fig. 14. Simulated and measured magnitude of the radar channel transfer function $\mathcal{R}$ in the yz-plane at $x = 0$ in the case of (a) a 24-GHz OWG, (b) a 24-GHz horn, and (c) a 61-GHz horn antenna. The colorbar spans a 30-dB dynamic range and its upper limit is set by the maximum simulated value.

Notwithstanding the more stringent examination of the derivation assumptions due to the reduced distance, a very good agreement between measurement and simulation results. Compared to the results in the xy-plane at $z = 500\,\text{mm}$, different characteristics of the radar channel are obtained. The reduced distance causes a different weighting of the integrand contributions by the antenna and, thus, different effective targets. Nonetheless, the strongly varying character of the transfer function is maintained.

B. Results for Variation in the xz- and the yz-Planes

To investigate the z-dependence, Figs. 13 and 14 present simulated and measured transfer function magnitudes for varying antenna positions in the xz-plane at $y = 0$ and in the yz-plane at $x = 0$, as indicated in Fig. 8(b) and (c), respectively. The z-range changes within $200\,\text{mm} < z < 500\,\text{mm}$ in a step size of 1 mm (0.5 mm) at 24 GHz (61 GHz). Here, the target-independent static offset is estimated by the center of the circle fitted to the reflection coefficients measured within a sliding window that contains nine consecutive samples along z-direction. The simulation predictions are well confirmed by measurements. The better agreement for the horn antenna measurements is due to reduced contribution of multipaths related to higher directivity. Inconsistencies between simulation and measurement are related to alignment and model uncertainties. Nonetheless, the agreement in terms of the qualitative response as well as the absolute magnitudes is very good.

The examples indicate that the classical far-field scattering based on a range-independent RCS is not applicable. With increasing distance, the receive power does not necessarily monotonically decrease. Conversely, approaching the target, local receive power minima arise, e.g., see Fig. 13(c) at $(x, y) = (-0.03\,\text{m}, 0.45\,\text{m})$, that may be several orders of magnitude below neighboring local maxima. An increased antenna directivity does not only lead to a corresponding power level increase, but it also changes the scattering characteristics. Furthermore, frequency significantly impacts the resulting spatial dependence of near-field scattering.

IV. Statistical Evaluation and Discussion

Following the results presented in Section III, the radar channel transfer function is subject to significant variations for changes of the antenna position. From practical viewpoint, the measurement position relative to the body is to some extent random as a particular alignment is infeasible due to the diversity and complex shape of the human body. In addition, even if the patient is asked not to move during measurement, unintentional small-scale movements as well as large-scale random body movements are inevitable. Accordingly, a statistical examination of the radar channel is purposeful to address the random character, which is inherent to the application. Assuming that vital-sign monitoring will be conducted over the chest region, the statistical analysis presented in the following considers the exemplary rectangular

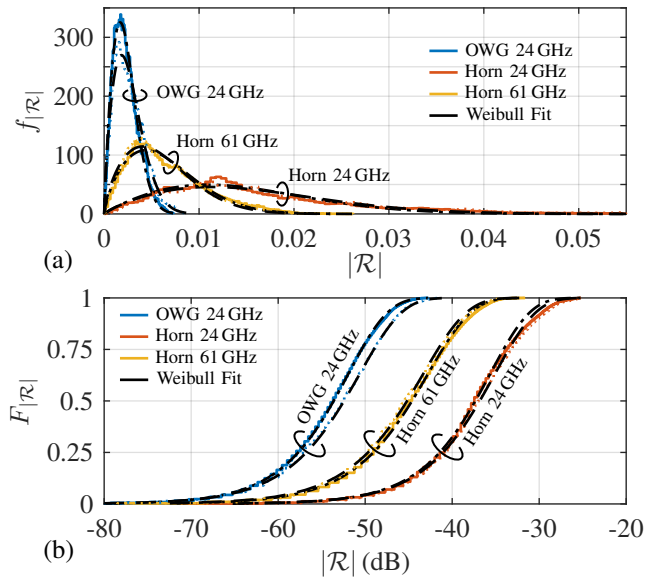

Fig. 15. (a) Histogram and (b) cumulative distribution of the radar channel transfer function at $z = 500\,\text{mm}$ based on simulation (dotted, colored), measurement (solid, colored), and the associated Weibull distribution fit calculated from simulated (dashed, black) and measured (dash-dotted, black) data.

window in the xy-plane at $z = 500\,\text{mm}$ highlighted in Fig. 8(a) with $-85\,\text{mm} < x < 115\,\text{mm}$ and $-60\,\text{mm} < y < 90\,\text{mm}$.

A. Receive Power Statistics

Given the simulated and measured radar channel transfer function, Fig. 15(a) evaluates the histograms of the magnitudes $f_{|\mathcal{R}|}$ within the observation window. The histograms use 100 bins uniformly distributed on linear scale from zero to the maximal value of $|\mathcal{R}|$. They are normalized such that their integrals equal unity (probability density function (PDF) normalization). Fig. 15(b) shows the corresponding cumulative distribution functions (CDF) $F_{|\mathcal{R}|}$ versus magnitude in dB. The measurement- and simulation-based distributions are in good agreement. Uncertainties of the antenna gain as a consequence of manufacturing tolerances contribute to the horizontal shifts between simulated and measured CDFs. The upper section of Table I lists the statistical parameters of the distributions. The increase in frequency with otherwise unchanged conditions (in particular directivity) approximately scales the mean and the median of the receive power in a proportion expected by the radar equation (8.1 dB). This approximately holds also for a change of directivity with other parameters fixed, however with a larger relative deviation (difference of 18 dB expected according to radar equation). The standard deviation (SD) evaluated on the dB-values (dB-SD) amounts to approximately 6 dB for all considered configurations.

The PDF of the magnitudes $f_{|\mathcal{R}|}$ within the considered rectangular window at $z = 500\,\text{mm}$ can be approximated by a Weibull distribution

$$f_\chi(\chi; A, B) = \frac{B}{A}\left(\frac{\chi}{A}\right)^{B-1} e^{-\left(\frac{\chi}{A}\right)^B} \tag{19}$$

where $A > 0$ is the scale parameter and $B > 0$ is the shape parameter. Fitting (19) to the histogram data yields the

TABLE I
STATISTICAL PARAMETERS OF TRANSFER FUNCTION $\mathcal{R}$ BASED ON MEASUREMENT AND SIMULATION RESULTS

Parameter	24 GHz OWG	24 GHz Horn	61 GHz Horn
$\text{mean}(\lvert\mathcal{R}\rvert)$ (dB)	-52.8 (-51.6)	-35.9 (-35.5)	-43.4 (-44.0)
$\text{median}(\lvert\mathcal{R}\rvert)$ (dB)	-53.6 (-52.4)	-37.3 (-36.7)	-44.6 (-45.2)
$\text{SD}[20\log_{10}(\lvert\mathcal{R}\rvert)]$	5.7 (6.1)	6.0 (6.0)	6.2 (6.2)
A (dB)	-51.9 (-50.6)	-35.6 (-35.1)	-42.8 (-43.3)
B (dB)	5.47 (4.9)	5.41 (5.15)	4.73 (4.63)
$I^{\text{dB}}_{0.25}$	7.4 (8.0)	7.4 (7.6)	8.0 (8.3)
$I^{\text{dB}}_{0.1}$	14.5 (15.0)	15.1 (15.3)	15.7 (15.7)
$I^{\text{dB}}_{0.01}$	28.2 (30.4)	30.1 (29.6)	30.9 (30.5)
$F_{A^{\text{dB}}_s}(A^{\text{dB}}_s > 3\,\text{dB})$ (%)	19.2 (14.1)	5.7 (4.8)	29.0 (24.7)
$F_{A^{\text{dB}}_s}(A^{\text{dB}}_s > 6\,\text{dB})$ (%)	5.9 (4.1)	1.5 (0.9)	9.8 (7.4)
$\text{mean}(A^{\text{dB}}_s)$	2.2 (1.8)	1.2 (1.1)	2.9 (2.6)
$\text{median}(A^{\text{dB}}_s)$	1.4 (1.2)	0.8 (0.7)	1.9 (1.7)
$\text{SD}(A^{\text{dB}}_s)$	2.7 (2.3)	1.6 (1.3)	3.2 (2.9)
$F_{\varphi_s}(\varphi_s > 10°)$ (%)	29.1 (18.2)	9.0 (7.8)	56.5 (54.2)
$F_{\varphi_s}(\varphi_s > 20°)$ (%)	9.0 (5.7)	2.3 (1.9)	17.4 (14.2)
$\text{mean}(\varphi_s)$ (°)	10.8 (8.4)	5.9 (5.6)	15.8 (14.6)
$\text{median}(\varphi_s)$ (°)	7.1 (5.6)	4.3 (4.2)	11.6 (11.1)
$\text{SD}(\varphi_s)$ (°)	14.8 (12.4)	8.1 (6.4)	17.9 (15.8)

Parameters based on simulation results in parentheses.

distribution parameters listed in Table I. The fitting results are included in Fig. 15, where the CDF for the Weibull distribution is given by

$$F_\chi(\chi; A, B) = 1 - \exp(-(\chi/A)^B). \tag{20}$$

The Weibull distribution reasonably matches with the simulated and measured histograms. The fit is less accurate for the 24-GHz horn toward higher magnitudes. The best accordance holds for the OWG. Note that, in general, the distribution will depend on the distance z.

To quantify the statistical spread of the receive power levels, the dB-inter-q-quantile range

$$I^{\text{dB}}_q = 20\log_{10}\left(\frac{F^{-1}_{|\mathcal{R}|}(1-q)}{F^{-1}_{|\mathcal{R}|}(q)}\right) \tag{21}$$

is evaluated in Table I for the quantiles $q = \{25\%, 10\%, 1\%\}$. As for the dB-SD, the dB-inter-q-quantile ranges are similar for the considered combinations of antennas and frequencies. The interpercentile ($q = 1\,\%$) range is in the order of 30 dB, which sets a requirement for the necessary dynamic range of the radar sensor to enable the feasibility of reliable vital-sign monitoring.

To account for the absorption losses due to skin, the distributions must be shifted toward lower power levels. Based on the discussion in Section II-B2, this can be approximated by the magnitude of the Fresnel reflection coefficient (14) at normal incidence $|\Gamma_H|_{\theta_i=0}|$. Taking the epidermis model [32] as an example, the power level shift evaluates to 3.5 dB and 4.4 dB at 24 GHz and 61 GHz, respectively.

B. Radar Channel Variability

As shown in Section III, the radar channel significantly varies already for small displacements of the relative antenna position in the xy-plane. These may be introduced by unintentional random small-scale movements of the patient

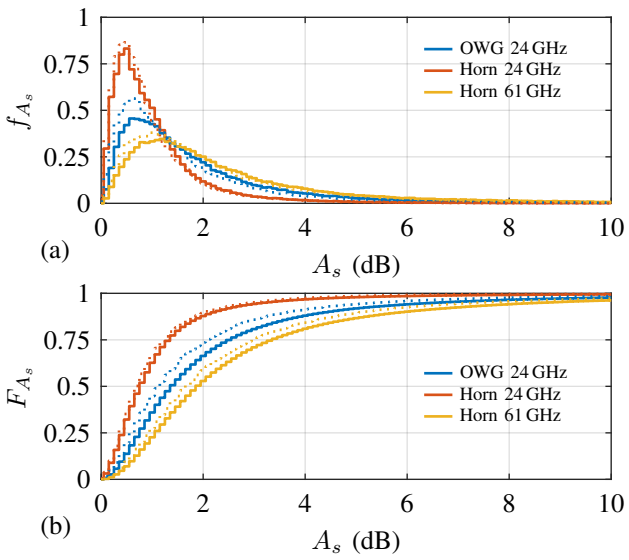

Fig. 16. (a) Histogram and (b) cumulative distribution of the magnitude dynamic range within a 1-mm quadratic sliding window based on measured (solid) and simulated (dotted) data.

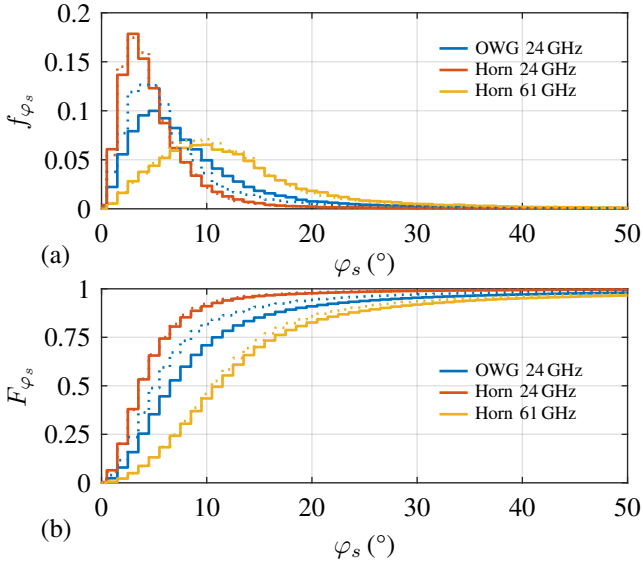

Fig. 17. (a) Histogram and (b) cumulative distribution of the phase dynamic range within a 1-mm quadratic sliding window based on measured (solid) and simulated (dotted) data.

during measurement. To quantify this effect, the variability of the transfer function within a small region around the current antenna position is statistically evaluated.

1) Magnitude Variability: The variability of the receive power level is quantified by

$$A_s^{\mathrm{dB}} = 20\log_{10}\left(\frac{\max\limits_{|\Delta_x|<\frac{s}{2},|\Delta_y|<\frac{s}{2}} |\mathcal{R}(x+\Delta_x, y+\Delta_y)|}{\min\limits_{|\Delta_x|<\frac{s}{2},|\Delta_y|<\frac{s}{2}} |\mathcal{R}(x+\Delta_x, y+\Delta_y)|}\right) \tag{22}$$

with $s > 0$ defining the size of a quadratic window around the antenna position (x, y, z). A_s^{dB} provides a measure of the local dynamic range of the receive magnitude. For the example of $s = 1\,\mathrm{mm}$, Fig. 16 evaluates the histogram of A_s^{dB} in terms of PDF $f_{A_s^{\mathrm{dB}}}$ and CDF $F_{A_s^{\mathrm{dB}}}$, where a bin width of 0.1 dB is selected. The middle section of Table I summarizes the key statistical parameters. The probability $F_{A_s^{\mathrm{dB}}}(A_s^{\mathrm{dB}} > 3\,\mathrm{dB})$ that the measured (simulated) magnitude varies by more than 3 dB within the 1-mm window amounts to 5.7 % (4.8 %) for the horn at 24 GHz, 19.2 % (14.1 %) for the OWG at 24 GHz, and 29 % (24.7 %) for the horn at 61 GHz. For the latter case, the magnitude varies more than 6 dB with a probability of 9.8 % (7.4 %). Because of its higher directivity, the horn antenna leads to less variability compared to the OWG. With increasing frequency the magnitude is less stable due to the larger electrical size of the target. These dependencies apply for the mean, the median, and the SD reported in Table I.

2) Phase Variability: The phase variability

$$\varphi_s = \max_{|\Delta_x|<\frac{s}{2},|\Delta_y|<\frac{s}{2}} \left|\mathrm{Arg}\left\{\frac{\mathcal{R}(x+\Delta_x, y+\Delta_y)}{\mathcal{R}(x,y)}\right\}\right| \tag{23}$$

within the s-wide quadratic window follows from the maximum phase change relative to the phase at the sampling point (x, y). $\mathrm{Arg}\{\cdot\}$ is the principal argument with an image $(-\pi, \pi]$. Fig. 17 evaluates the corresponding PDF f_{φ_s} and CDF F_{φ_s} for $s = 1\,\mathrm{mm}$, where the bin width is 1°. The qualitative dependencies of the phase variability on directivity and frequency are comparable to those for the magnitude. The probability $F_{\varphi_s}(\varphi_s > 10°)$ that the measured (simulated) relative phase varies by more than 10° within the 1-mm window amounts to 9.0 % (7.8 %) for the horn at 24 GHz, 29.1 % (18.2 %) for the OWG at 24 GHz, and 56.5 % (54.2 %) for the horn at 61 GHz. The lower section of Table I lists further statistical properties.

V. Conclusion

The radar channel transfer function in vital-sign sensing applications strongly varies with the relative antenna position. This is the result of operating in the radiative near field of the electrically large human body target and the associated scattering phenomena, which depend on frequency as well as antenna directivity. Focusing on the analysis of scattering effects at mmWave frequencies, human skin can be simplified by PEC without altering the fundamental character of the radar channel. It can be analyzed and accurately simulated by a physical-optics-based approach, whose applicability is confirmed by extensive measurements. Because of the variablilty of the radar channel and the inherent random character of the application, a statistical evaluation provides a comprehensive representation of the radar channel features. Small shifts of relative alignment between the antenna and the human body, which in a practical application inevitably occur during monitoring, may introduce significant modulations of both magnitude and phase of the receive signal. Their likelihood depends on frequency and antenna directivity. As a consequence, the detection of time-critical vital-sign features such as individual heart beats can be impeded. Thus, near-field scattering effects set a physical limitation regarding the robustness of continuous radar-based vital-sign sensing irrespective of particular radar architectures and signal processing techniques.

ACKNOWLEDGMENT

The authors would like to thank their colleague Nils Bade for his outstanding support in implementing the automated measurement setup: *AntRig-Measurement-System* (https://github.com/NilsBade/AntRig-Measurement-System).

REFERENCES

[1] J. E. Kiriazi, O. Boric-Lubecke, and V. M. Lubecke, "Considerations in measuring vital signs cross section with Doppler radar," in *Proc. IEEE Radio Wireless Symp.*, Phoenix, AZ, USA, Jan. 2011, pp. 426–429.

[2] E. Antolinos and J. Grajal, "Improving vital signs monitoring in real-world environments with W-band phased-array radars," *IEEE Trans. Microw. Theory Techn.*, vol. 73, no. 8, pp. 4363–4374, Aug. 2025.

[3] N. C. Albrecht, M. Heyer, M. Wenzel, D. Langer, H. Lu, and A. Koelpin, "Long-distance heart sound detection using 122 GHz CW radar with 3D printed high-gain antennas," in *Proc. IEEE Radio Wireless Symp. (RWS)*, Las Vegas, NV, USA, Feb. 2023, pp. 34–36.

[4] M. Wenzel, B. Tegowski, N. C. Albrecht, D. Langer, and A. Koelpin, "Heart sound detection using an ultra-wideband FMCW radar," in *Proc. IEEE/MTT-S Int. Microw. Symp. (IMS)*, San Diego, CA, USA, 2023, pp. 1192–1195.

[5] C. Will *et al.*, "Radar-based heart sound detection," *Sci. Rep.*, vol. 8, no. 11551, Jul. 2018.

[6] M. Wenzel, D. Langer, A. Koelpin, and F. Lurz, "A modular 61 GHz vital sign sensing radar system for long-term clinical studies," in *Proc. IEEE Topical Conf. Wireless Sensors Sensor Netw. (WiSNeT)*, San Antonio, TX, USA, Jan. 2024, pp. 18–21.

[7] N. C. Albrecht *et al.*, "EmRad: Ubiquitous vital sign sensing using compact continuous-wave radars," *IEEE Open J. Eng. Med. Biol.*, vol. 5, pp. 725–734, 2024.

[8] J.-M. Muñoz-Ferreras, Z. Peng, R. Gómez-García, and C. Li, "Review on advanced short-range multimode continuous-wave radar architectures for healthcare applications," *IEEE J. Electromagn., RF, Microw. Med. Biol.*, vol. 1, no. 1, pp. 14–25, Jun. 2017.

[9] C. Li, V. M. Lubecke, O. Boric-Lubecke, and J. Lin, "A review on recent advances in doppler radar sensors for noncontact healthcare monitoring," *IEEE Trans. Microw. Theory Techn.*, vol. 61, no. 5, pp. 2046–2060, May 2013.

[10] M. Wenzel, N. C. Albrecht, D. Langer, M. Heyder, and A. Koelpin, "Catch your breath! Vital sign sensing with radar," *IEEE Microw. Mag.*, vol. 24, no. 3, pp. 75–82, Mar. 2023.

[11] E. Antolinos and J. Grajal, "Comprehensive comparison of continuous-wave and linear-frequency-modulated continuous-wave radars for short-range vital sign monitoring," *IEEE Trans. Biomed. Circuits Syst.*, vol. 17, no. 2, pp. 229–245, Apr. 2023.

[12] J.-Y. Park *et al.*, "Preclinical evaluation of a noncontact simultaneous monitoring method for respiration and carotid pulsation using impulse-radio ultra-wideband radar," *Sci. Rep.*, vol. 9, no. 11892, Aug. 2019.

[13] S. Abadpour, S. Marahrens, M. Pauli, J. Siska, N. Pohl, and T. Zwick, "Backscattering behavior of vulnerable road users based on high-resolution RCS measurements," *IEEE Trans. Microw. Theory Techn.*, vol. 70, no. 3, pp. 1582–1593, Mar. 2022.

[14] B. Tegowski, D. Langer, M. Wenzel, N. C. Albrecht, and A. Koelpin, "Near-field scattering phenomena in monostatic radar applications derived from physical optics," *IEEE Trans. Antennas Propag.*, vol. 73, no. 2, pp. 1084–1094, 2025.

[15] C. Will *et al.*, "Local pulse wave detection using continuous wave radar systems," *IEEE J. Electromagn. RF Microw. Med. Biol.*, vol. 1, no. 2, pp. 81–89, Dec. 2017.

[16] A. Prat, S. Blanch, A. Aguasca, J. Romeu, and A. Broquetas, "Collimated beam FMCW radar for vital sign patient monitoring," *IEEE Trans. Antennas Propag.*, vol. 67, no. 8, pp. 5073–5080, Aug. 2019.

[17] X. Li *et al.*, "Dynamic electromagnetic model to detect human vital signs based on time-domain finite integration theorem," *IEEE J. Electromagn. RF Microw. Med. Biol.*, vol. 9, no. 2, pp. 240–250, Jun. 2025.

[18] G. Ortiz-Jimenez, F. Garcia-Rial, L. A. Ubeda-Medina, R. Pages, N. Garcia, and J. Grajal, "Simulation framework for a 3-D high-resolution imaging radar at 300 GHz with a scattering model based on rendering techniques," *IEEE Trans. THz Sci. Technol.*, vol. 7, no. 4, pp. 404–414, Jul. 2017.

[19] K. Williams, L. Tirado, Z. Chen, B. Gonzalez-Valdes, J. A. Martinez, and C. M. Rappaport, "Ray tracing for simulation of millimeter-wave whole body imaging systems," *IEEE Trans. Antennas Propag.*, vol. 63, no. 12, pp. 5913–5918, Dec. 2015.

[20] J. E. Kiriazi, O. Boric-Lubecke, and V. M. Lubecke, "Modeling of human torso time-space characteristics for respiratory effective RCS measurements with Doppler radar," in *IEEE MTT-S Int. Microw. Symp. Dig.*, Baltimore, MD, USA, Jun. 2011, pp. 1–4.

[21] J. G. Meana, J. Á. Martinez-Lorenzo, F. Las-Heras, and C. Rappaport, "Wave scattering by dielectric and lossy materials using the modified equivalent current approximation (MECA)," *IEEE Trans. Antennas Propag.*, vol. 58, no. 11, pp. 3757–3761, Nov. 2010.

[22] G. T. Ruck, *Radar Cross Section Handbook*. New York, NY, USA: Plenum Press, 1970.

[23] L. Corucci, E. Giusti, M. Martorella, and F. Berizzi, "Near field physical optics modelling for concealed weapon detection," *IEEE Trans. Antennas Propag.*, vol. 60, no. 12, pp. 6052–6057, Dec. 2012.

[24] T. Malherbe, R. D'Errico, C. Delaveaud, and P. Pouliguen, "Evaluation of human body scattering in near and far field by iterative physical optics for mmWave sensing applications," in *Proc. 19th Eur. Conf. Antennas Propag. (EuCAP)*, Stockholm, Sweden, Mar. 2025, pp. 1–4.

[25] B. Tegowski, D. Langer, N. C. Albrecht, and A. Koelpin, "Fast determination of the monostatic radar channel in the near-field of electrically large targets," in *Proc. 55th Eur. Microw. Conf. (EuMC)*, Utrecht, Netherlands, Sep. 2025, pp. 610–613.

[26] P. Pouliguen and L. Desclos, "A new analytical solution of physical optics for near field mono or bistatic applications," in *IEEE Antennas Propag. Soc. Int. Symp. Dig.*, Chicago, IL, USA, Jun. 1992, pp. 396–399.

[27] P. Pouliguen and L. Desclos, "A physical optics approach to near field RCS computations," *Annales Des Télécommun.*, vol. 51, no. 5-6, pp. 219–226, May 1996.

[28] Y. Gao and R. Zoughi, "Millimeter wave reflectometry and imaging for noninvasive diagnosis of skin burn injuries," *IEEE Trans. Instrum. Meas.*, vol. 66, no. 1, pp. 77–84, Jan. 2017.

[29] M. Chen, C.-C. Chen, S. Y.-P. Chien, and R. Sherony, "Artificial skin for 76–77 GHz radar mannequins," *IEEE Trans. Antennas Propag.*, vol. 62, no. 11, pp. 5671–5679, Nov. 2014.

[30] S. Gabriel, R. W. Lau, and C. Gabriel, "The dielectric properties of biological tissues: II. Measurements in the frequency range 10 Hz to 20 GHz," *Phys. Med. Biol.*, vol. 41, no. 11, pp. 2251–2269, Nov. 1996.

[31] S. Gabriel, R. W. Lau, and C. Gabriel, "The dielectric properties of biological tissues: III. Parametric models for the dielectric spectrum of tissues," *Phys. Med. Biol.*, vol. 41, no. 11, pp. 2271–2293, Nov. 1996.

[32] K. Sasaki, K. Wake, and S. Watanabe, "Measurement of the dielectric properties of the epidermis and dermis at frequencies from 0.5 GHz to 110 GHz," *Phys. Med. Biol.*, vol. 59, no. 16, pp. 4739–4747, Aug. 2014.

[33] D. M. Pozar, *Microwave Engineering*, 4th ed. Hoboken: Wiley, 2012.

[34] N. C. Albrecht, J. P. Weiland, D. Langer, M. Wenzel, and A. Koelpin, "Characterization of the influence of clothing and other materials on human vital sign sensing using mmWave radar," in *Proc. 53rd Eur. Microw. Conf. (EuMC)*, 2023, pp. 428–431.

[35] B. Tegowski and A. Koelpin, "Accuracy limitations of interferometric radar owing to the radar cross section of its antenna," *IEEE Trans. Microw. Theory Techn.*, vol. 72, no. 7, pp. 4317–4324, Jul. 2024.

[36] B. Tegowski and A. Koelpin, "Calibration of the self-radar-cross-section of continuous-wave radars," *IEEE Trans. Microw. Theory Techn.*, vol. 73, no. 9, pp. 6029–6036, Sep. 2025.

Bartosz Tegowski was born in 1997. He received the B.Sc. and M.Sc. degrees in electrical engineering from the Hamburg University of Technology, Hamburg, Germany, in 2019 and 2021, respectively, where he is currently pursuing the Ph.D. degree at the Institute of High-Frequency Technology.

His current research interests include microwave filter design, electromagnetic theory, modeling of near-field scattering, and radar systems for medical and industrial applications.

Mr. Tegowski was a recipient of the Science Award of the Gisela and Erwin Sick Foundation and the First Prize from the 3D-Printed Surface-Mounted Filter Student Design Competition of the IEEE International Microwave Symposium in 2023. He received the Best Student Paper Award of the German Microwave Conference in 2024, the Young Scientist Award of the International Radar Symposium in 2025, and the Young Engineer Prize of the European Microwave Conference in 2025. He serves as a reviewer for the IEEE MICROWAVE AND WIRELESS TECHNOLOGY LETTERS.

Dominik Langer (Graduate Student Member, IEEE) received the B.Sc. and M.Sc. degrees in electrical engineering from the Hamburg University of Technology, Hamburg, Germany, in 2018 and 2021, respectively, where he is currently pursuing the Ph.D. degree at the Institute of High-Frequency Technology.

His current research interests include antenna design, additive manufacturing, and interferometric radar systems.

Mr. Langer was a recipient of the First Prize of the Radar for Noncontact Vital Sign Sensing of the IEEE International Microwave Symposium in 2021, 2022, and 2023, respectively. He serves as a reviewer for the IEEE MICROWAVE AND WIRELESS TECHNOLOGY LETTERS.

Nils C. Albrecht (Graduate Student Member, IEEE) received the B.Sc. and M.Sc. degrees from Hamburg University of Technology, Hamburg, Germany, in 2018 and 2021, respectively, where he is currently pursuing the Ph.D. degree at the Institute of High-Frequency Technology.

His current research interest include radar systems for medical applications, software-defined radar, and machine learning for radar signals.

Mr. Albrecht was a recipient of the First Prize of the Radar for Noncontact Vital Sign Sensing of the IEEE International Microwave Symposium in 2021, 2022, and 2023, respectively. Additionally, he received the Science Award of the Gisela and Erwin Sick Foundation. He serves as a reviewer for IEEE TRANSACTIONS ON RADAR SYSTEMS and IEEE OPEN JOURNAL OF ENGINEERING IN MEDICINE AND BIOLOGY.

Alexander Koelpin (Fellow, IEEE) received the Diploma degree in electrical engineering and the Ph.D. and Habilitation degrees from the University of Erlangen–Nuremberg (FAU), Erlangen, Germany, in 2005, 2010, and 2014, respectively.

From 2005 to May 2017, he was with the Institute for Electronics Engineering, FAU. From 2007 to 2010, he was a Team Leader, from 2010 to 2015, a Group Leader of Circuits, Systems, and Hardware Test, and since 2015, he has been a Leader of the Group Electronic Systems. From June 2017 to February 2020, he was a Professor and the Head of the Chair for Electronics and Sensor Systems with the Brandenburg University of Technology Cottbus–Senftenberg, Cottbus, Germany. Since March 2020, he has been with the Hamburg University of Technology, Hamburg, Germany, as a Professor and the Head of the Institute of High-Frequency Technology. He has authored or coauthored more than 300 publications in his areas of interest. He serves as a reviewer for several journals and conferences. His research interests are in the areas of microwave circuits and systems, radar and wireless sensing, wireless communication systems, local positioning, and six-port technology.

Dr. Koelpin was a member of the Commission A: Electromagnetic Metrology of U.R.S.I. from 2012 to 2017. He has been an Elected Member since 2018 and has been the Vice Chair of the IEEE MTT-S/AP German Chapter Executive Board since 2020. He has received the IEEE MTT-S Outstanding Young Engineer Award in 2016, the ITG Award of the German VDE in 2017, and the IEEE Microwave Application Award in 2025. He was the Chair of the IEEE MTT-S Technical Committee MTT-24, from 2018 to 2020. He served as the Conference Co-Chair for the IEEE Topical Conference on Wireless Sensors and Sensor Networks, the Conference Chair for the 2020 German Microwave Conference, the Technical Program Chair for IEEE Radio and Wireless Week 2021, and the General Chair for IEEE Radio and Wireless Week 2023.